A tiny host galaxy for the first giant black hole: z = 7.5 quasar in BlueTides

Ananth Tenneti, Stephen Wilkins, Tiziana Di Matteo, Rupert A C Croft, Yu Feng

Published in
Monthly Notices of the Royal Astronomical Society

Link to external publisher version
https://doi.org/10.1093/mnras/sty3161

Monthly Notices
of the
ROYAL ASTRONOMICAL SOCIETY

MNRAS **483,** 1388–1399 (2019)
Advance Access publication 2018 November 22

doi:10.1093/mnras/sty3161

A tiny host galaxy for the first giant black hole: $z = 7.5$ quasar in BlueTides

Ananth Tenneti [1★], Stephen M. Wilkins [2★], Tiziana Di Matteo,[1★] Rupert A. C. Croft[1] and Yu Feng[3]

[1]*McWilliams Center for Cosmology, Department of Physics, Carnegie Mellon University, Pittsburgh, PA 15213, USA*
[2]*Department of Physics and Astronomy, University of Sussex, Brighton BN1 9QH, UK*
[3]*Berkeley Center for Cosmological Physics, Department of Physics, University of California Berkeley, Berkeley, CA 94720, USA*

Accepted 2018 November 16. Received 2018 November 16; in original form 2018 May 31

ABSTRACT

The most distant known quasar recently discovered by Bañados et al. is at $z = 7.5$. We explore the host galaxy of the brightest quasar in the large-volume cosmological hydrodynamic simulation BlueTides. The brightest quasar in BlueTides has a luminosity of $\sim$ a few $10^{13}\,L_\odot$ and black hole mass of $6.4 \times 10^8\,M_\odot$ at $z \sim 7.5$, comparable to the observed quasar. The quasar resides in a rare halo of mass $M_H \sim 10^{12}\,M_\odot$ and has a host galaxy of stellar mass $4 \times 10^{10}\,M_\odot$ with an ongoing (intrinsic) star formation rate of $\sim 80\,M_\odot\,yr^{-1}$. The corresponding intrinsic ultraviolet (UV) magnitude of the galaxy is roughly 2.7 mag fainter than the quasar's magnitude and the galaxy is highly metal enriched with mean metallicity equal to the solar value. We derive the quasar and galaxy spectral energy distribution in the mid- and near-infrared *JWST* bands. Finally, we predict a significant amount of dust attenuation in the rest-frame UV corresponding to $A_{1500} \sim 1.7$, giving a UV-based star formation rate of $\sim 14\,M_\odot\,yr^{-1}$. We present mock *JWST* images of the galaxy in different MIRI and NIRCam filters. The host galaxy is detectable in NIRCam filters, but is extremely compact ($R_E = 0.35$ kpc). It will require *JWST*'s exquisite sensitivity and resolution to separate the galaxy from the central point source.

Key words: hydrodynamics – methods: numerical – galaxies: high-redshift – early Universe.

1 INTRODUCTION

There are many unsolved problems in our quest to understand the first billion years of cosmic structure formation and the formation of the first galaxies and black holes. Supermassive black holes, as massive as those in galaxies today, are known to exist in the early Universe, even up to $z \sim 7$. Luminous, extremely rare, quasars at $z \sim 6$ have been discovered in the Sloan Digital Sky Survey (Fan et al. 2006; Jiang et al. 2009) and, until recently, the highest redshift quasar known was (Wu et al. 2015) at $z = 7.09$ (Mortlock et al. 2011).

Katz et al. (1994) used numerical simulations to predict the existence of a potential quasar site at $z = 8$. Using the MassiveBlack simulation, performed in a box of size 0.75 Gpc, Di Matteo et al. (2012) studied the formation of $10^9\,M_\odot$ black holes at $z \sim 7$. The quasar luminosity functions and quasar clustering in the MassiveBlack simulation are found to be consistent with observational constraints at high redshifts (DeGraf et al. 2012). The basic properties of the quasar hosts, such as the star formation rate (SFR) and estimates of molecular gas in the galaxies, are also found to be consistent with observations at $z \sim 6$ (Khandai et al. 2012).

Excitingly, Bañados et al. (2018; hereafter B18) reported the discovery of a bright quasar at $z = 7.54$, J1342+0928, which is currently the record-holder for known high-redshift quasars. The observed quasar is found to have a bolometric luminosity of $4 \times 10^{13}\,L_\odot$ and an inferred black hole mass of $8 \times 10^8\,M_\odot$. However, the properties of the galaxy hosting this quasar are currently completely unknown. In this paper, we focus on predicting the host galaxy properties of such a luminous and massive early quasar using the cosmological hydrodynamic simulation BlueTides (Feng et al. 2016). More specifically, we make predictions for the spectral energy distributions (SEDs) of the quasar host galaxy and the active galactic nucleus (AGN) in the *James Webb Space Telescope* (*JWST*) (Gardner et al. 2006; Kalirai 2018) filters. In a companion paper (Ni et al. 2018), we study the feedback around the most luminous quasar, and in particular the properties of the outflow gas in the host halo of the quasar.

The upcoming launch of *JWST* will facilitate the observational study of the properties of a large number of high-redshift galaxies at $z \sim 8$–10. In particular, *JWST* will make observations in the

★ E-mail: vat@andrew.cmu.edu (AT); S.Wilkins@sussex.ac.uk (SMW); tiziana@phys.cmu.edu (TDM)

rest-frame optical/near-infrared (NIR) wavelengths of high-redshift galaxies, including the massive quasar host galaxies. Volonteri et al. (2017) predicted the properties of high-redshift galaxies and AGNs in *JWST* bands by developing a population synthesis model based on empirical relations. The volume and resolution of the BlueTides simulation facilitate a direct study of AGN and host galaxy properties of rare objects such as most massive quasars at high redshifts ($z \sim 7.5$). In this paper, we compare the SEDs of galaxies that are directly calculated based on the stellar age and metallicity with the quasar's SED obtained based on the luminosity and accretion rate.

Recently, Venemans et al. (2017) reported observations from IRAM/NOEMA and JVLA to obtain some constraints on the host galaxy of the quasar, J1342 +0928 of B18. The dynamical mass of the host is determined to be $<1.5 \times 10^{11}\,M_\odot$ and SFRs are in the range 85–545 $M_\odot\,yr^{-1}$. Venemans et al. (2017) also report a dust mass of 0.6–4.3 $\times\ 10^8\,M_\odot$ and a metal-enriched gas ($\sim 5 \times 10^6\,M_\odot M_{C+}$) with an implied stellar mass of $\sim 2 \times 10^{10}\,M_\odot$

This paper is organized as follows. In Section 2, we provide the details of the Bluetides-II simulation along with the methods to identify galaxies and compute SEDs. In Section 3, we provide details of the properties of the most luminous quasar and its host galaxy in BT-II. We show the distribution of gas, dark matter, and stellar matter in BT-II corresponding to a region of the *JWST* field of view (FOV) in Section 4. In Section 5, we discuss the AGN and host galaxy SEDs along with their band luminosities in the *JWST* filters. The mock *JWST* images of the host galaxy, sampled at the *JWST* resolution and including point spread function (PSF) effects of the filters, are shown in Section 6. Finally, we conclude in Section 7.

2 BLUETIDES-II SIMULATION

The BlueTides simulation (Feng et al. 2016) was the first phase in the BlueTides project, and involved the evolution of a cosmological volume to $z = 8$. In this paper, we report on some of the first results from BlueTides-II (BT-II), the second phase of the project, which continued the evolution of the BlueTides volume to redshifts $z < 8$. Here we focus on redshifts $z = 7.5$–8, close to the redshift of the J1342+0928 quasar in B18.

2.1 MP-GADGET SPH code

Both phases of the BlueTides simulation have been performed using the smoothed particle hydrodynamics (SPH) code MP-GADGET[1] (Feng et al. 2016) in a cubical periodic box of volume $(400\,h^{-1}\,\mathrm{Mpc})^3$. The simulation was evolved from initial conditions at $z = 99$ with 2×7040^3 dark matter and gas particles and a gravitational softening length equal to $\varepsilon_{\rm grav} = 1.5\,h^{-1}\,\mathrm{Kpc}$. The cosmological parameters in the simulation were chosen according to those in the *WMAP* 9-year data release (Hinshaw et al. 2013). The cosmological parameters are as follows: cosmological constant density parameter $\Omega_\Lambda = 0.7186$, mass density parameter $\Omega_{\rm Matter} = 0.2814$, baryon density parameter $\Omega_{\rm Baryon} = 0.0464$, amplitude of matter fluctuations $\sigma_8 = 0.820$, spectral index $\eta_s = 0.971$, and Hubble parameter $h = 0.697$. The details of phase I of the simulation and various properties of the simulated galaxies till $z = 8$ are described in Feng et al. (2016).

We provide a brief description of the feedback model adopted in the BlueTides simulation. The MP-GADGET code adopts the pressure–entropy formulation of SPH (pSPH) (Read, Hayfield & Agertz 2010; Hopkins 2013) to solve the Euler equations. Star formation is implemented based on the multiphase star formation model (Springel & Hernquist 2003) and also includes several modifications following Vogelsberger et al. (2013). The gas cooling is modelled based on radiative processes (Katz, Weinberg & Hernquist 1996) and also via metal cooling (Vogelsberger et al. 2014). The formation of molecular hydrogen and its effect on star formation at low metallicities is modelled according to the prescription by Krumholz & Gnedin (2011). A Type II supernova wind feedback model (Okamoto et al. 2010), which assumes that the wind speeds are proportional to the local one-dimensional dark matter velocity dispersion, is also incorporated. Finally, the black hole growth and feedback from AGNs is incorporated based on the supermassive black hole model developed in Di Matteo, Springel & Hernquist (2005).

[1] https://github.com/MP-Gadget/MP-Gadget

2.2 Galaxies

We identify galaxies from the snapshots of BT-II using a friends of friends (FOF) algorithm (Davis et al. 1985) with linking length 0.2 times the mean interparticle separation. We have shown in Feng et al. (2016) that at these redshifts, there is a good correspondence between FOF-defined objects and galaxies selected using SExtractor (Bertin & Arnouts 1996) from mock imaging. In earlier papers (Feng et al. 2016; Waters et al. 2016; Wilkins et al. 2017), the high-redshift galaxy properties predicted by BlueTides, including the star formation density, stellar mass function, and ultraviolet (UV) luminosity function, are found to match the observational constraints at $z = 8, 9, 10$. In the simulation at redshift $z = 7.5$, there are 4.7×10^5 galaxies with stellar mass $>5 \times 10^7\,M_\odot$.

Each galaxy contains from $60 - 2.3 \times 10^5$ star particles, each with an age and metallicity. We use the information from these to compute spectra for the galaxies, and also for the visualization of galaxy images in different bands.

2.3 Galaxies' spectral energy distributions

The spectral energy distribution of the AGN host is constructed by attaching the SED of a simple stellar population (SSP) to each star particle based on its mass, age, and metallicity. Specifically we employ version 2.1 of the Binary Population and Spectral Populations Synthesis (SPS) (BPASS; Eldridge et al. 2017) model utilizing a modified Salpeter initial mass function (Salpeter high-mass slope with a break at $<0.5\,M_\odot$) and a high-mass cut-off of $300\,M_\odot$. See Wilkins et al. (2016) for a discussion of the impact of assuming alternative SPS models. Attenuation by dust is modelled for each star particle individually by determining the line of density of metals and assuming a linear relation to the dust optical depth. This is calibrated to reproduce the bright end of the rest-frame UV luminosity function at $z \sim 8$ (see Wilkins et al. 2017).

2.4 Quasar spectrum

The spectral energy distribution of the AGN is determined by the black hole mass and accretion rate using the functional form of the spectrum adopted in the spectral synthesis code CLOUDY (Ferland et al. 2013), given by

$$f_\nu = \nu^{\alpha_{\rm UV}} e^{-\frac{h\nu}{kT_{\rm BB}}} e^{-\frac{kT_{\rm IR}}{h\nu}} + a\nu^{\alpha_x}, \quad (1)$$

where $\alpha_{\rm UV} = -0.5$, $\alpha_X = -1$, and $kT_{\rm IR} = 0.01\,\mathrm{Ryd}$. We note that this procedure to obtain the theoretical AGN spectrum is the same as the method used in Volonteri et al. (2017).

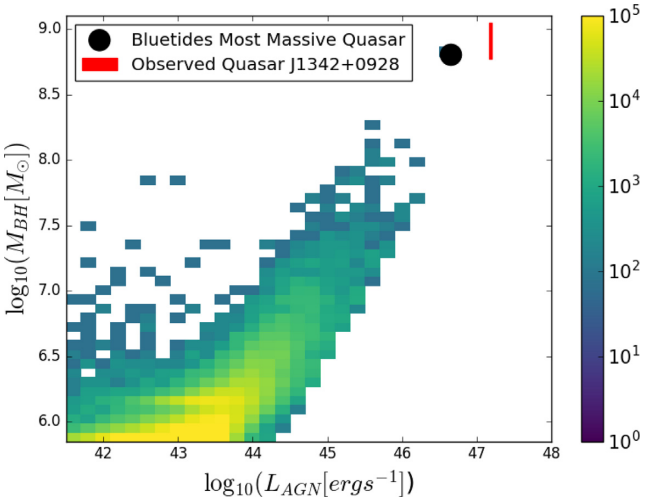

Figure 1. The bolometric luminosity of AGNs in the BT-II simulation at redshift $z = 7.6$ plotted against black hole mass. The solid black circle is plotted at the position of the most luminous quasar in BT-II, which we study in detail in this paper, along with its host galaxy. The red line shows the relevant information for the observed $z = 7.54$ quasar, J1342+0928, of B18. The height of the line corresponds to the observational uncertainty. The colour bar indicates the number density of galaxies.

2.5 The most luminous quasar in BlueTides-II

The quasar J1342+0928 found by B18 was discovered using data that cover a significant fraction of the sky. Three large-area surveys were used, the *Wide-field Infrared Survey Explorer* (ALLWISE), the United Kingdom Infrared Telescope Infrared Deep Sky Survey (UKIDSS) Large Area Survey, and the DECam Legacy Survey (DECaLS).[2] The overlap between these is up to 4000 square degrees, which leads to a potential search volume of up to 5.5 $(\mathrm{Gpc}\,h^{-1})^3$ between $z = 7.5$ and $z = 8$. Although the BlueTides volume is large for a cosmological hydrodynamic simulation, the observational search volume could be up to two orders of magnitude larger. This should be kept in mind when comparing the simulation and observational results. When searching for a luminous quasar in the simulation, however, we do allow ourselves to search over a slightly wider redshift range than the single snapshot $z = 7.54$ corresponding to the observed quasar's redshift. Because of the variability in black hole accretion, and therefore quasar luminosity, by picking a redshift where the luminosity is high we are increasing the effective simulation volume.

We choose the object in BT-II to compare to the B18 quasar, J1342+0928, on the basis of its luminosity. In Fig. 1, we show black hole mass against AGN luminosity for the entire simulation at redshift $z = 7.6$. We can see that there is a clear relationship between the two quantities, and also that the brightest AGN also has the most massive black hole. The black hole mass, accretion rate, and other parameters related to the host galaxy are given in Table 1. The black hole mass is within the 1σ observational uncertainty quoted by B18, and its luminosity is smaller by a factor of $\sim$3.4. Although not in perfect agreement, we note that BT-II is the only cosmological hydrodynamic simulation with full physics of galaxy formation that has a luminous quasar that is in closest agreement to the J1342+0928 quasar. BT-II is the only simulation with the volume and resolution suitable for studying supermassive black holes at high redshifts with the black hole mass and luminosity comparable to those of J1342+0928. So, we choose the object with the highest luminosity and black hole mass in BT-II to make predictions. We study this black hole and its host galaxy in the rest of the pape.

Over the redshift range $z = 7.5$–8 that we consider, the black hole is growing, as can be seen in Fig. 2. The accretion rate is between 1 and $10\,\mathrm{M}_\odot\,\mathrm{yr}^{-1}$, with variations of a factor of 2 or 3 over time-scales of $\sim$50 Myr. These variations are large compared to the observational error on the B18 quasar luminosity, indicating that there is no need for the simulation quasar luminosity to be an exact match. The simulated black hole's accretion rate does appear to be slowing down over the range plotted, which can also be seen as the flatter trend of black hole growth in the top panel. This is consistent with the quasar's surroundings having been affected by AGN feedback. We study this feedback in more detail for the same simulated object in a companion paper (Ni et al. 2018).

Table 1. Properties of the most luminous quasar in BlueTides and the quasar's host galaxy from z = 8 to z = 7.54.

Property	$z = 8$	$z = 7.85$	$z = 7.6$	$z = 7.54$
$M_{\rm BH}$ ($\times 10^8\,\mathrm{M}_\odot$)	4.1	5.2	6.4	6.7
D/T	0.19	0.20	0.14	0.13
$L_{\rm BH}$ ($\times 10^{12}\,\mathrm{L}_\odot$)	5.7	5.9	11.8	3.6
$\dot{M}_{BH}$ ($\mathrm{M}_\odot\,\mathrm{yr}^{-1}$)	3.8	4.0	7.9	2.5
SFR ($\mathrm{M}_\odot\,\mathrm{yr}^{-1}$)	67.80	73.19	82.55	83.96
$M_{\rm Halo}$ ($\times 10^{11}h^{-1}\,\mathrm{M}_\odot$)	5.9	6.1	9.1	9.4
M_{200} ($\times 10^{11}h^{-1}\,\mathrm{M}_\odot$)	3.7	3.9	4.3	4.4
$M_{\rm star}$ ($\times 10^{10}\,\mathrm{M}_\odot$)	3.75	3.86	4.18	4.23
$M_{\rm gas}$ ($\times 10^{10}h^{-1}\,\mathrm{M}_\odot$)	4.9	4.8	9.3	9.5
$f_{\rm gas}\left(\frac{M_{\rm gas}}{M_{\rm gas}+M_{\rm star}}\right)$	0.65	0.64	0.76	0.76

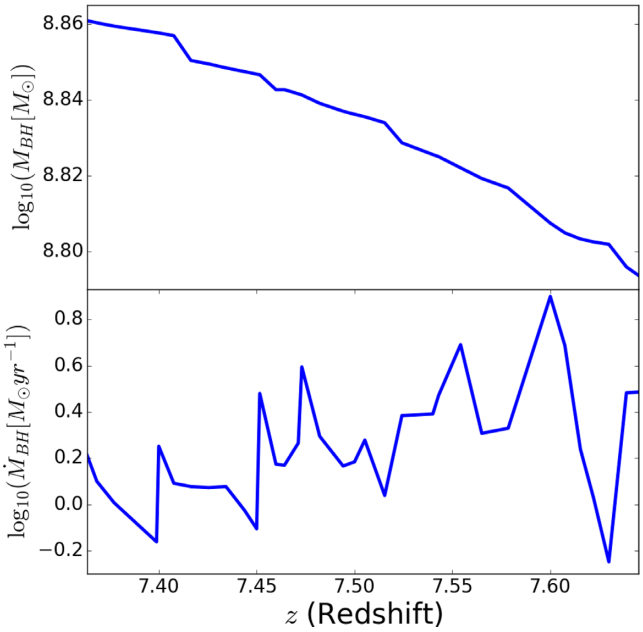

Figure 2. Redshift evolution of the black hole mass (*top*), and black hole accretion rate.

[2] http://legacysurvey.org/decamls

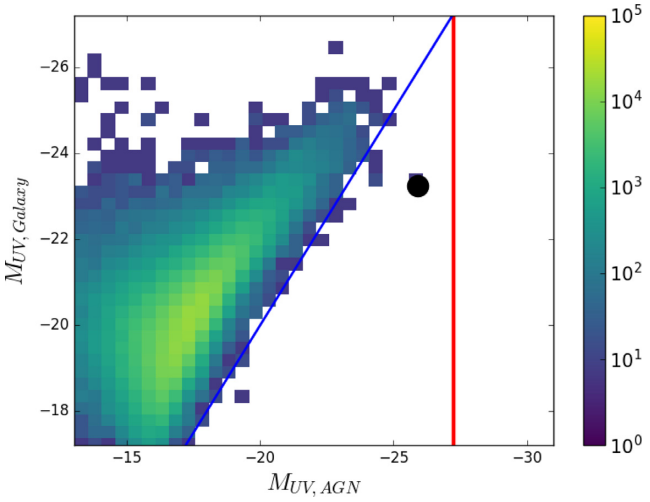

Figure 3. The absolute magnitude of AGNs in the BTII simulation at redshift $z = 7.6$ plotted against galaxy absolute magnitude. The solid black circle is plotted at the position of the most luminous quasar in BT-II. The red line shows the observed luminosity of the J1342+0928 quasar in B18.The solid blue line shows where the galaxy and AGN are equally luminous. The host galaxy is predicted to have $M_{\rm UV} = -23.24$. The colour bar indicates the number density of galaxies.

3 QUASAR AND GALAXY PROPERTIES

The most luminous AGN in BT-II at $z \sim 7.5$ is hosted by a galaxy with FoF halo mass $\sim 10^{12}\,{\rm M}_\odot$ and stellar mass $4 \times 10^{10}\,{\rm M}_\odot$ (see Table 1). Given that BT-II has only one counterpart to the J1342+0928 quasar, it is not possible to quantify the uncertainty in the galaxy properties of the quasar host in the simulation. In an earlier study (Di Matteo et al. 2017), the basic host galaxy properties of the four most massive black holes in the BlueTides simulation and their environments are discussed at $z = 8$. The host galaxy of the most luminous AGN in BT-II is however not the most massive galaxy in the volume, as can be seen from the top panel of Fig. 4, where we show the stellar mass of all galaxies against AGN luminosity. There are about 10 other galaxies with stellar masses that are similar or greater, including some with AGN luminosities 5 orders of magnitude smaller. The most massive galaxy has a stellar mass ∼5 times larger than the host of the most luminous AGN.

When considering galaxy luminosity, the quasar host is even less exceptional, which can be seen in Fig. 3. Here we plot the absolute rest-frame UV magnitude of the AGNs and their host galaxies. We can see that the host of brightest AGN is about 3 mag fainter than the brightest galaxies in BT-II. Only a handful of galaxies lie to the right of the $M_{\rm UV,AGN} = M_{\rm UV,Galaxy}$ line, indicating that the vast majority of accreting black holes do not outshine their hosts. The main locus of points in Fig. 3 is approximately 3 mag to the left of (fainter than) the $M_{\rm UV,AGN} = M_{\rm UV,Galaxy}$ line, indicating that for most galaxies the AGN is 3 mag fainter than the galaxy. The brightest quasar is the opposite, on the other hand, being about 3 mag more luminous than its host.

The galaxy UV luminosity is closely related to the SFR. The SFR of the host galaxy is computed from the sum of the SFRs of all particles in the halo. From the middle panel of Fig. 4 we can see that the SFR of the brightest quasar host is about 1 order of magnitude smaller than the most star forming. The star formation history of this host galaxy does include episodes of much higher activity. For example, in fig. 3 of Di Matteo et al. (2017), the same galaxy is

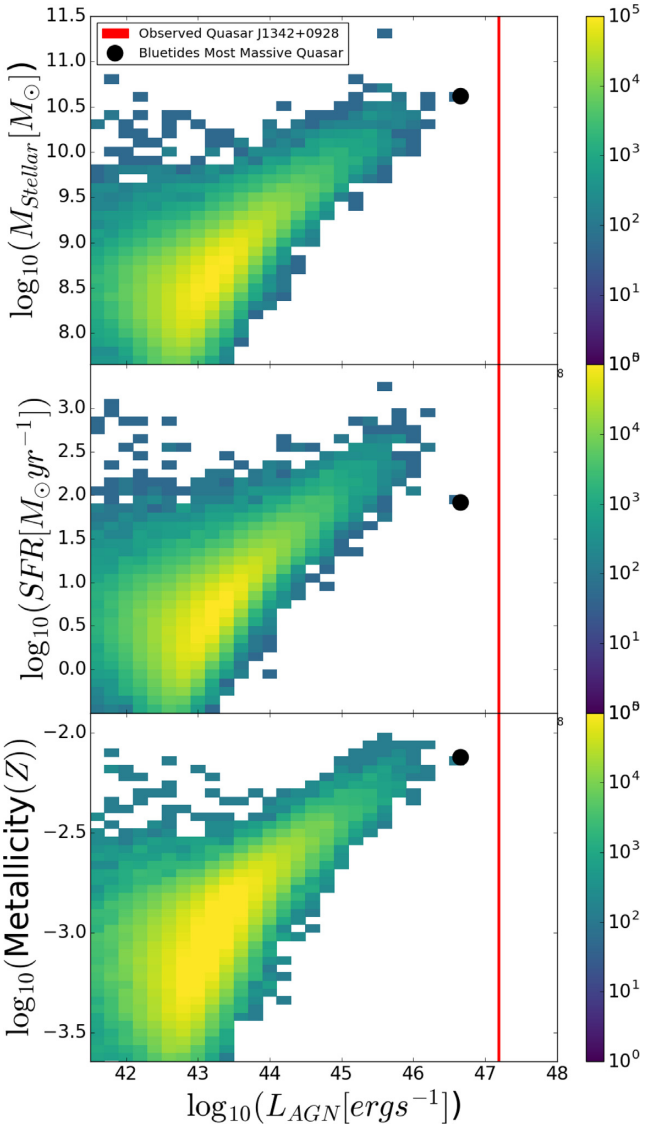

Figure 4. Properties of the host galaxy for the brightest quasar. *From top to bottom*: The stellar mass, $M_\odot$, the star formation rate (SFR), and the stellar metallicities of the galaxies in BTII at $z = 7.6$. The most massive/luminous object is indicated by a solid black point in previous figures. The colour bar indicates the number density of galaxies.

shown at much higher redshifts, where at $z = 10$, the SFR was as high as $300\,{\rm M}_\odot\,{\rm yr}^{-1}$. Even at redshifts closer (within $\Delta z \sim 0.5$) to the one we are considering, the SFR was an order of magnitude higher, as we see below (Fig. 5).

Fig. 4 also shows the stellar mass of the galaxies as a function of AGN luminosity. In this case, the AGN host is again in the top few galaxies, consistent with the fact that it underwent a very significant earlier burst of star formation. This star formation episode resulted in metal production, which is evident in the bottom panel of Fig. 4, where it is also among the top few galaxies by mean metallicity (computed from the star particles). We note that the solar metallicity is defined to be $Z_\odot = 0.02$ in the simulation.

We show the SFR as function of redshift over the interval of interest in the middle panel of Fig. 5. The sampling is relatively coarse in time because of the timing of the simulation snapshots, but we can see that it has varied by a factor of around 2 over the

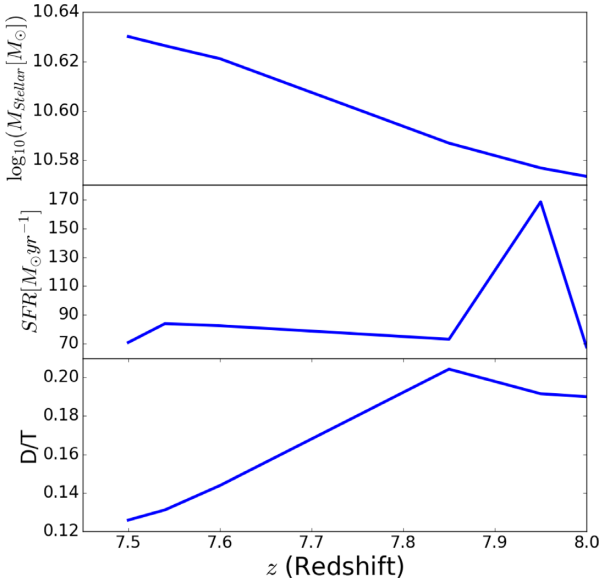

Figure 5. The host galaxy's stellar mass (*top*), star formation rate (*middle*), and the disc to total ratio (*bottom*) as a function of redshift.

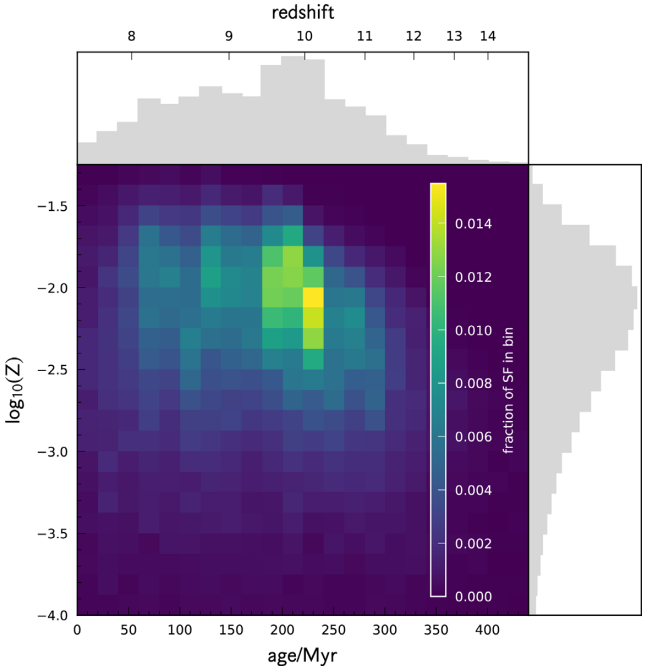

Figure 6. The metallicity of star particles in the quasar host galaxy as a function of their age (or equivalently formation redshift). Solar metallicity is $Z = 0.02$.

150 Myr before $z = 7.5$. The growth in the stellar mass of the galaxy is shown in the top panel.

We have also computed the galaxy's disc to total (D/T) ratio using star particle kinematics. We have used a standard technique (Governato et al. 2007) to determine the fraction of stars in each galaxy that are on planar circular orbits and that are associated with a bulge. In Di Matteo et al. (2017; where more details are given), we found that the majority of massive galaxies at these high redshifts are discs. In fact, at $z = 8$, 70 per cent of galaxies above a mass of 10^{10} M$_\odot$ were kinematically classified as discs (using the standard threshold of the D/T ratio of 0.2; Governato et al. 2007). In the present case, the quasar host galaxy is below this threshold, and is becoming even less disc-like towards lower redshifts. Some of the galaxies in Di Matteo et al. (2017) were extremely disc-like in visual appearance as well as kinematically. As we shall see later (Section 6.1), this galaxy is not. This is consistent with the general expectation for galaxies hosting the most massive black holes, which are often in areas with low tidal fields (Di Matteo et al. 2017) and are less likely to be discs.

With the large number of particles in the quasar host galaxy, the metallicity of the stars as a function of age can be examined in detail. We do this in Fig. 6, where we show a two-dimensional histogram of these properties. The median metallicity of the stars that formed at redshifts $z > 12$ can be seen to be about $log_{10}(Z) \simeq -2.5$ and this increases to $\log_{10}(Z) \simeq -1.75$ by redshift $z = 8$. As expected for these early sites of vigorous star formation (e.g. Walter et al. 2003; Maiolino et al. 2005; Wang et al. 2011, 2013; Venemans et al. 2016), the median metallicity is high, reaching solar values for stars forming at $z \sim 9$. The burst of star formation at $z \sim 10$ in this galaxy can be clearly seen in the age histogram above the main plot, and also as a concentration of pixels in the main panel at these redshifts and metallicity $\log_{10}(Z) \simeq -2.1$.

4 LARGE-SCALE ENVIRONMENT: THE *JWST* FIELD OF VIEW

The most luminous quasar in BT-II is located in a high-density environment, which will make it an interesting target for observations of the surrounding sky area. We are most interested in follow-up observations with the *JWST*, and in this section we present images of the dark matter, gas, and stellar in the entire *JWST* field of view, before concentrating on mock images of the host galaxy in detail in Section 6. stellar matter.

JWST's Mid-Infrared Instrument (MIRI) and Near Infrared Camera (NIRCam) have different FOV sizes. The NIRCam instrument has two modules, each with an FOV of 132 arcsec × 132 arcsec with filters in the wavelength range 0.6–5.0 μm. MIRI has an FOV of 74 arcsec × 113 arcsec and provides broadband imaging in the wavelength range 5.0–27.0 μm. The physical scale corresponding to 1 arcsec at $z = 7.6$ is 5.1 kpc, so the NIRCam and MIRI FOVs are approximately $4\,h^{-1}$ Mpc across their longest dimensions. We therefore choose to plot images of a $4\,h^{-1}$ Mpc × $4\,h^{-1}$ Mpc simulation. We also restrict ourselves to a depth of $4\,h^{-1}$ Mpc to only show physically associated structure. The volume considered is therefore 10^{-6} of the entire BT-II simulation box.

4.1 Gas and dark matter

In Fig. 7 (left-hand panel), we plot the distribution of gas in this region of $4\,h^{-1}$ Mpc centred on the most massive black hole in the BT-II simulation. The filamentary structure of the gas is readily visible, with the quasar itself lying at the intersection of four filaments. The distribution of matter is visually fairly symmetric around the centre, indicating that the asymmetry in the tidal field will be fairly low, consistent with the low D/T ratio of the host galaxy (Di Matteo et al. 2017). The gas in the image is colour coded by temperature, with the intergalactic medium (IGM) far from the galaxy being at a temperature of $\sim 10^4$ K. The BT-II simulation includes a patchy model for reionization, but such a high-density region has already been reionized (heating the IGM to this temperature) by this redshift. The red-orange colour of the gas close to the quasar indicates that it has been heated by AGN feedback to temperatures of

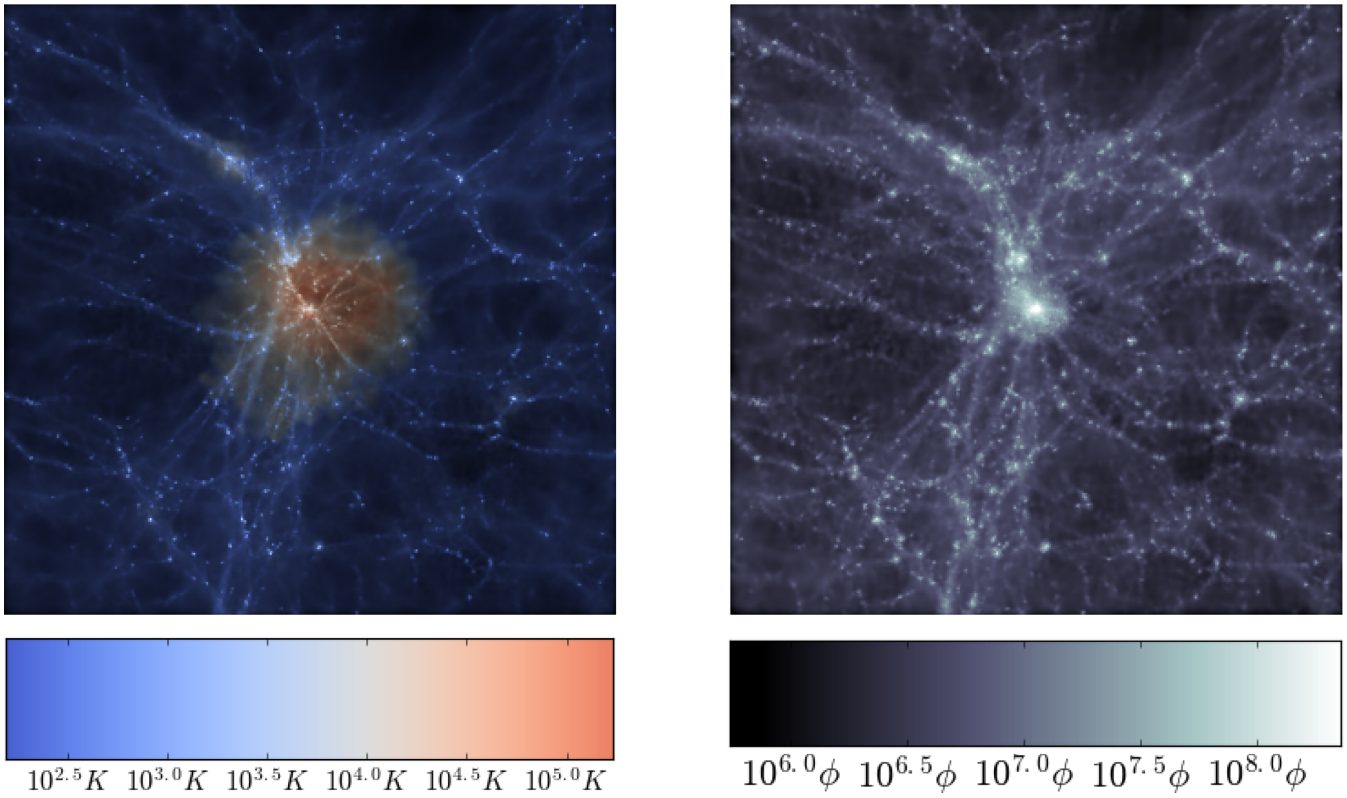

Figure 7. Images showing the distribution of gas and dark matter in the region centred on the most massive black hole of size $4\,h^{-1}$ Mpc corresponding to the *JWST* field of view at $z = 7.6$. *Top left*: distribution of gas where the intensity of the blue region represents the density and the colour scale represents the temperature of the gas. *Top right*: the corresponding dark matter density with the colour bar given in units of ϕ ($M_\odot$ Mpc^{-2}).

10^6–10^7 K. This feedback and the associated winds are studied in more detail in Ni et al. (2018).

The dark matter distribution around the quasar (Fig. 7, left-hand panel) traces the gas distribution, as expected. A large filament is more visible in dark matter than gas, entering from the top left, and in general throughout the image many subhaloes are visible along the filaments.

4.2 Stars

An interesting question we would like to address is whether any companion galaxies are expected close to the location of the highest redshift quasar. Deep *JWST* imaging may be able to detect close neighbours or even satellite galaxies. In Fig. 8, the intensity of the red region represents the stellar density. We also label the rest-frame UV magnitudes of the three most luminous galaxies in the region. Here, the galaxy with the most massive black hole has the highest luminosity in this field of view with an $M_{\rm UV} = -23$. We can see two more luminous galaxies, one slightly above this galaxy with a magnitude of $M_{\rm UV} = -21.2$ and another further above on the left with a magnitude of $M_{\rm UV} = -20.7$. The second brightest galaxy is within 300 kpc of the quasar in projected separation and the host haloes seen in the figure are close to merging.

If the extinction for the other galaxies is assumed to be the same as for the quasar host galaxy, then their luminosities will be fainter by 1.5 mag for each galaxy . The extinct UV magnitudes of the galaxies labelled in the figure will therefore be -21.5, -19.7, and -19.2 respectively in decreasing order of their luminosities. All three of the galaxies visible and labelled in Fig. 7 (right-hand panel) would be visible in *JWST* imaging, for example using *JWST*'s NIRCam F070W filter (see below) and an apparent magnitude limit of $m_{AB} \sim 28$ for an integration time[3] of 10 ks. The galaxy with the most massive black hole has an apparent magnitude of $m_{AB} = 24.1$. The other two labelled galaxies visible in this FOV have magnitudes of $m_{AB} = 26.9$ and $m_{AB} = 27.5$.

5 QUASAR AND GALAXY SPECTRAL ENERGY DISTRIBUTIONS

We determine the luminosities of the quasar host galaxy in each *JWST* MIRI and NIRCam filter by summing the spectral energy distributions of each star particle computed from the method described in Section 2.3 and convolved with the given filter. The SED of the quasar is obtained using the spectral synthesis code CLOUDY (Ferland et al. 2013) based on the black hole mass and accretion rate as described in Section 2.4. The rest-frame quasar spectrum is shown in the left-hand panel of Fig. 9. Here, we show both the AGN continuum (green lines) and the emission spectrum (black line). The filter responses of the different mid- and near-IR *JWST* bands in the quasar rest frame are also shown at the bottom of the plot. We can see that the peak of the AGN SED is captured by the NIR filters, as is the Lyman break and Lyman-alpha absorption.

The AGN outshines the host galaxy considerably in all *JWST* wavebands. In the left-hand panel of Fig. 9, the SED of the quasar is compared against the galaxy spectrum obtained by summing the individual SEDs of star particles in the galaxy. We show both the

[3]https://jwst-docs.stsci.edu/display/JTI/NIRCam + Sensitivity

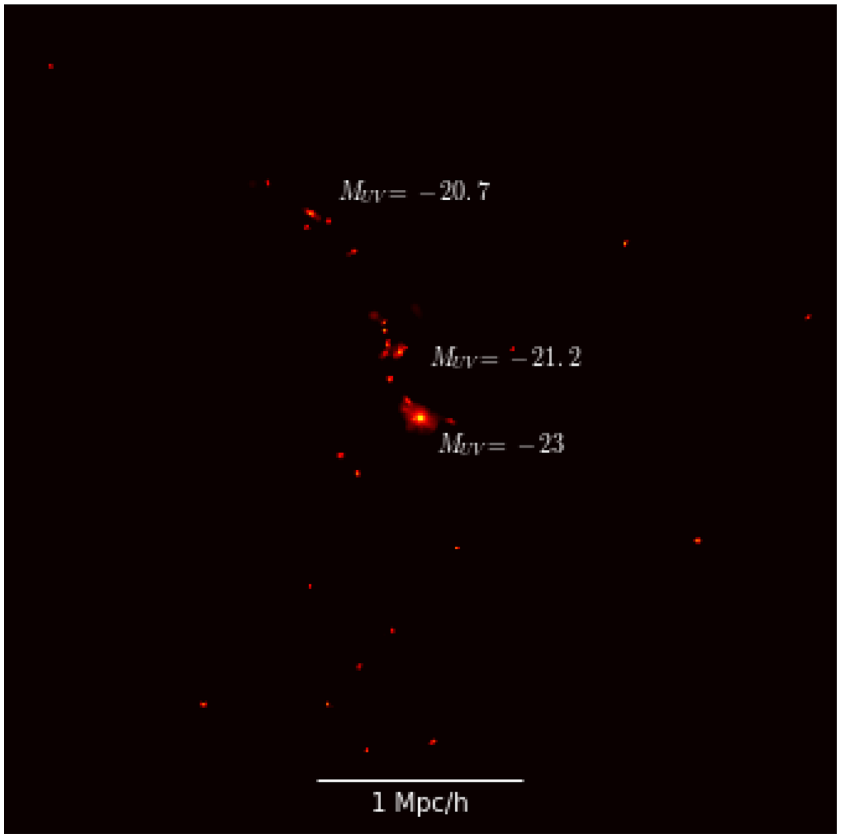

Figure 8. Galaxies in the field of view of *JWST*. Stellar densities are shown increasing from red to yellow. The labels indicate the absolute magnitudes of the three brightest galaxies in the rest-frame UV.

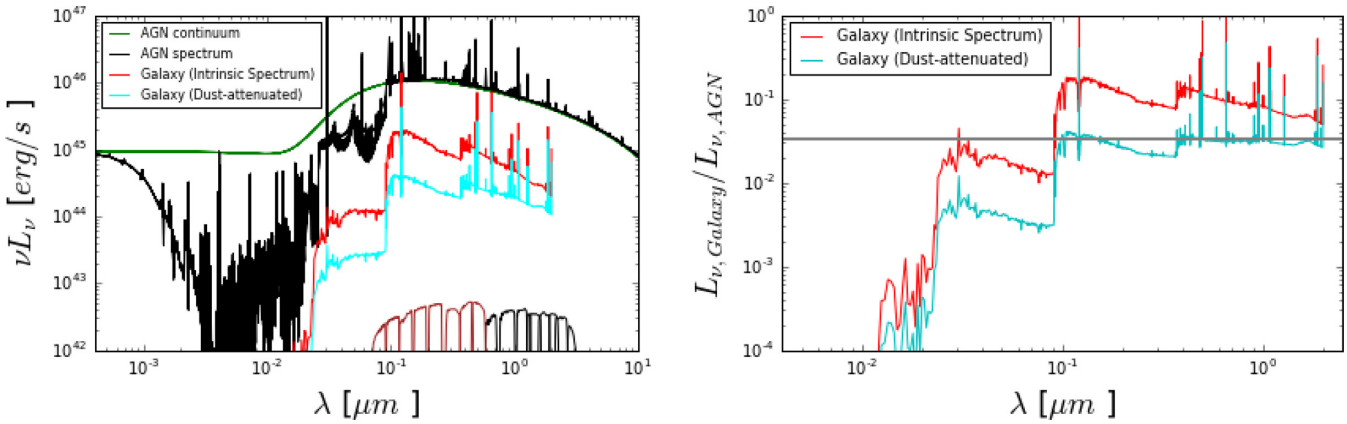

Figure 9. *Left*: The figure shows the SEDs of AGNs and the star particles in the galaxy hosting the brightest quasar at $z = 7.6$. The green and black lines show the continuum and emission spectrum of the quasar obtained from the CLOUDY software. The red line shows the galaxy's intrinsic spectrum obtained by summing the individual SEDs of star particles in the galaxy. The cyan line shows the dust-attenuated spectrum of the galaxy. *Right*: The figure shows the ratio of the galaxy luminosity to that of the AGN as a function of wavelength. The red and cyan lines correspond to the intrinsic and dust-attenuated spectrum of the galaxy, respectively. The grey horizontal line represents the value at the which the AGN luminosity is about 30 times brighter than the galaxy luminosity.

galaxy's intrinsic spectrum (red line) and the dust-attenuated spectrum (cyan line). To understand the relative brightness of the host galaxy when compared with that of its quasar at different wavelengths, we plot the ratio of the SEDs of the galaxy and the quasar in the right-hand panel of Fig. 9. As seen from the figure, at rest-frame wavelengths above 0.5 μm, the dust-attenuated luminosity of the galaxy is smaller than that of the quasar by up to a factor of ∼30. More specifically, the dust attenuation in the rest-frame UV gives an extinction $A_{1500} \sim 1.7$ and, compared to the SFR based on the intrinsic stellar UV luminosity of $\mathrm{SFR_{int}}(L_{1500}) \sim 65\,\mathrm{M_\odot\ yr^{-1}}$, the resulting SFR based on the attenuated stellar UV luminosity $\mathrm{SFR_{obs}}(L_{1500}) \sim 14\,\mathrm{M_\odot\ yr^{-1}}$.

We focus in more detail on the NIR part of the spectrum in Fig. 10, where we plot the observed-frame monochromatic luminosities of

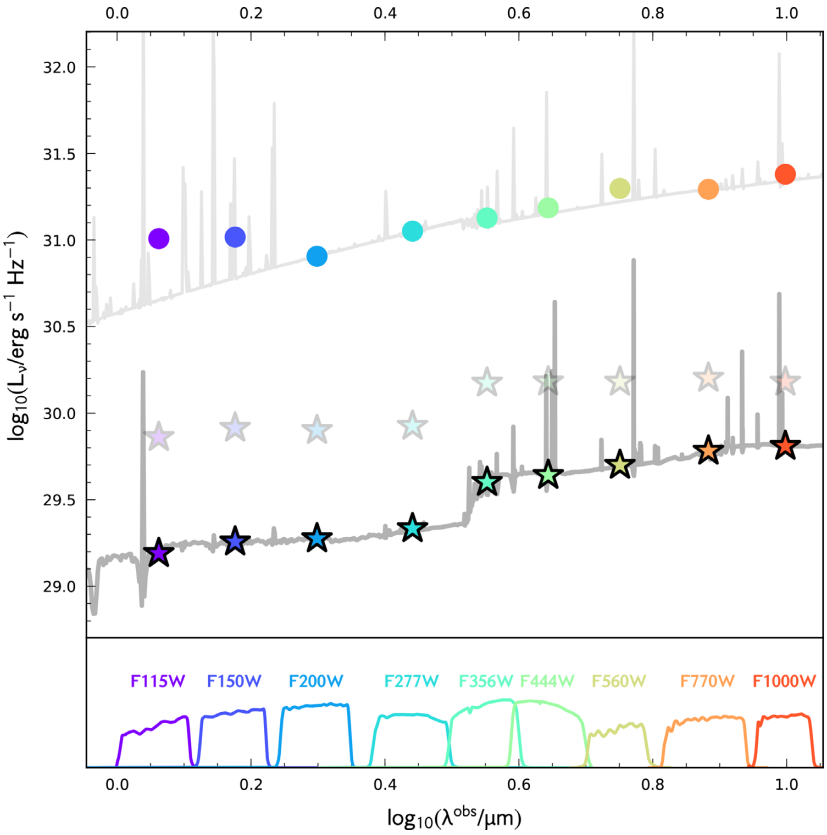

Figure 10. The top panel in the figure shows the observed-frame spectra of the brightest quasar (grey line) and the host galaxy (black line). The bottom panel shows the filter curves of *JWST*'s NIRCam F115W, F150W, F200W, F277W, F356W, F444W filters and MIRI F560W, F770W, F1000W filters. The corresponding band luminosities of the quasar (circular markers) and the host galaxy (star markers) are shown at the mean wavelengths in the top panel.

the quasar and galaxy as a function of wavelength. At observed wavelengths above 3 μm (NIRCam F356W, F444W filters, MIRI F560W, F770W, F1000W filters), the luminosities are separated by ∼1.5 dex. Point source subtraction techniques are slightly more likely to be successful at long wavelengths. Based on the galaxy–AGN luminosity ratio, this is likely to be challenging if the host galaxy of the observed quasar, J1342+0928, in B18 is similar to the equivalent host in the simulation.

6 MOCK *JWST* IMAGES OF HOST GALAXY

With an angular resolution of ∼0.1 arcsec, *JWST* will be able to image the host galaxy of J1342 + 0928. The BT-II simulation has a resolution (force softening) of 250 pc at this redshift, which corresponds to 0.05 arcsec, so the simulation is well matched to the potential of *JWST* and can be used to predict how the galaxy will appear in *JWST* imaging. Here, we first show native images (without convolution with telescope angular or spectral characteristics) and then move on to mock *JWST* images of the individual host galaxy of the bright quasar at $z = 7.6$.

6.1 Native images without PSF convolution and filter selection

Before plotting the images of the galaxy in different *JWST* filters, we show the distribution of only the stellar component of the galaxy in the left-hand panel of Fig. 11. The image shows a region of width 10 kpc in physical units. The inner circle in the images has a radius of 1 kpc, while the outer circle is of radius 5 kpc, corresponding to a size of 1 arcsec. We note that the galaxy is centrally concentrated, but it is visible out to ∼8 kpc. It is ellipsoidal and rather featureless. We show only one orientation, but the other views are similar – it exhibits no flattening or disc-like structure.

As we move from the left- to right-hand panels of Fig. 11, the intensity of the pixels in the images represents the distribution of stellar mass, intrinsic UV luminosity, observed UV luminosity (i.e. with dust attenuation), and observed-frame *R*-band luminosity, respectively. We note that the effects of the PSF and the contribution from the quasar luminosity are not included here. The effects of dust attenuation are clearly visible in the two middle panels. We have already seen in Fig. 10 that dust can decrease the relevant luminosity by a factor of ∼5–10. Given that the luminosity and black hole mass of the observed quasar, J1342+0928, in B18 are extremely high, it is unlikely to be very attenuated. So, here we assume that the dust attenuation can be ignored for the quasar luminosity.

6.2 Mock *JWST* images in NIRcam and MIRI filters

We show mock *JWST* images of the host galaxy of the brightest quasar in Figs 12 and 13 where the luminosity has been computed using the individual band luminosities of the star particles in the NIRCam and *JWST* filters. All the mock *JWST* images shown in Figs 12 and 13 are of width 10 kpc in physical units and the PSFs for these images were generated using the WEBBPSF PYTHON package (Perrin et al. 2015).

In Fig. 12, the luminosities were obtained from the dust-attenuated SEDs of the star particles. The figure shows the galaxy

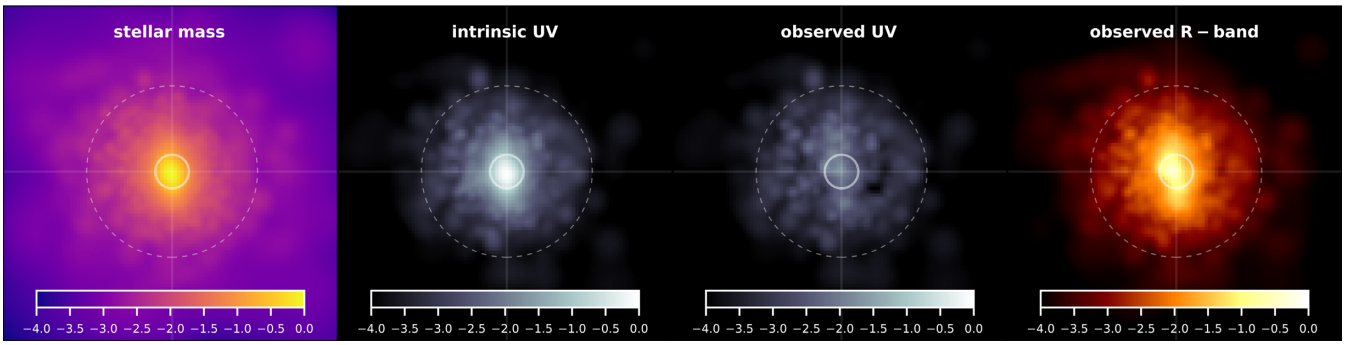

Figure 11. Images of the host galaxy of the brightest quasar in a region of size 10 kpc in physical units with a resolution of 0.1 kpc. The inner circle is of radius 1 kpc (0.2 arcsec) and the outer circle depicts a radius of 5 kpc (1 arscsec). From left to right, the images show the distribution of stellar mass, intrinsic UV-band luminosity, observed UV-band luminosity, and observed *R*-band luminosity. The colour scale is logarithmic and ranges from $1e-4I_{\rm max}-I_{\rm max}$, where $I_{\rm max}$ is the maximum intensity of the pixel for the stellar mass and intrinsic UV images. The $I_{\rm max}$ for the observed UV and observed *R*-band images are based on the $I_{\rm max}$ of the intrinsic UV image.

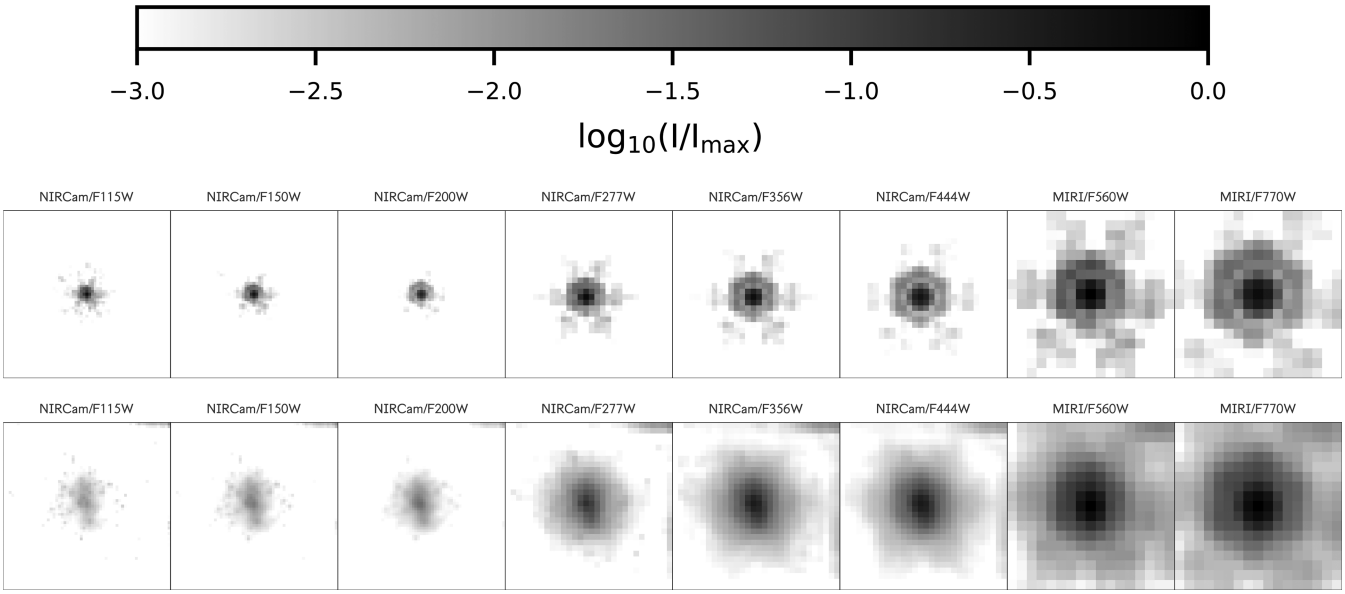

Figure 12. Dust-attenuated mock *JWST* images. We show the host galaxy of the brightest quasar, plotting the distribution of dust-attenuated luminosities of star particles in NIRCam's F115W, F150W, F200W, F277W, F356W, F444W filters and MIRI's F560W, F770W filters. The images show a region of size 10 kpc in physical units, sampled at the *JWST* resolution of $0.032-0.111$ arcsec, depending on the filter and include the effects of the PSF. The top panel shows the images with the contribution from AGN luminosity included. The bottom-panel images have do not have AGN. The intensity scale is logarithmic, varying from 0.1 per cent of the maximum intensity, $I_{\rm max}$, up to the maximum intensity, as indicated by the colour bar.

image in each of the NIRCam filters F115W, F150W, F200W, F277W, F356W, F444W and MIRI filters F560W, F770W. In the top panel of the figure, the images show the combined luminosity from the AGN and stellar component, when taking the relevant filter-dependent PSF effects into account. These images can be compared with those in the bottom panel, where only the distribution of stellar luminosity in the galaxy is plotted after convolution with the PSF, and AGN contribution is not included. As expected, when the AGN is included the AGN dominates in all filters. The full width at half-maximum of the PSF is approximately in the range $0.04-0.145$ arcsec, increasing as we go to longer wavelengths for the NIRCam filters shown, and $\sim 0.2-0.25$ arcsec for the MIRI filters. Comparison of the top and bottom rows reveals that the PSF is indeed much more centrally concentrated than the galaxy light, indicating that point source subtraction should be possible in principle. The colour scale is different in the top and bottom rows (in order to make the galaxy visible in the bottom row), so the galaxy in the top row is largely below the lower end of the scale (but it is included, together with the AGN). The elliptical shape of the galaxy in the bottom panels can be compared to that in the native images (e.g. of the stellar mass distribution) in Fig. 11, indicating that if AGN subtraction is carried out it may be possible to extract this aspect of the galaxy morphology from observations.

It is obvious from Fig. 12 that the galaxy is extremely compact. In order to give a quantitative value for the galaxy effective radius $R_{\rm e}$, we first exclude star particles >10 kpc away from the centre of the galaxy. We find the exact centre by minimizing the second moment of the smoothed galaxy image. We then compute the galaxy size using a pixel-based technique (summing the area of the brightest pixels that sum to 50 per cent of the total light). This yields an

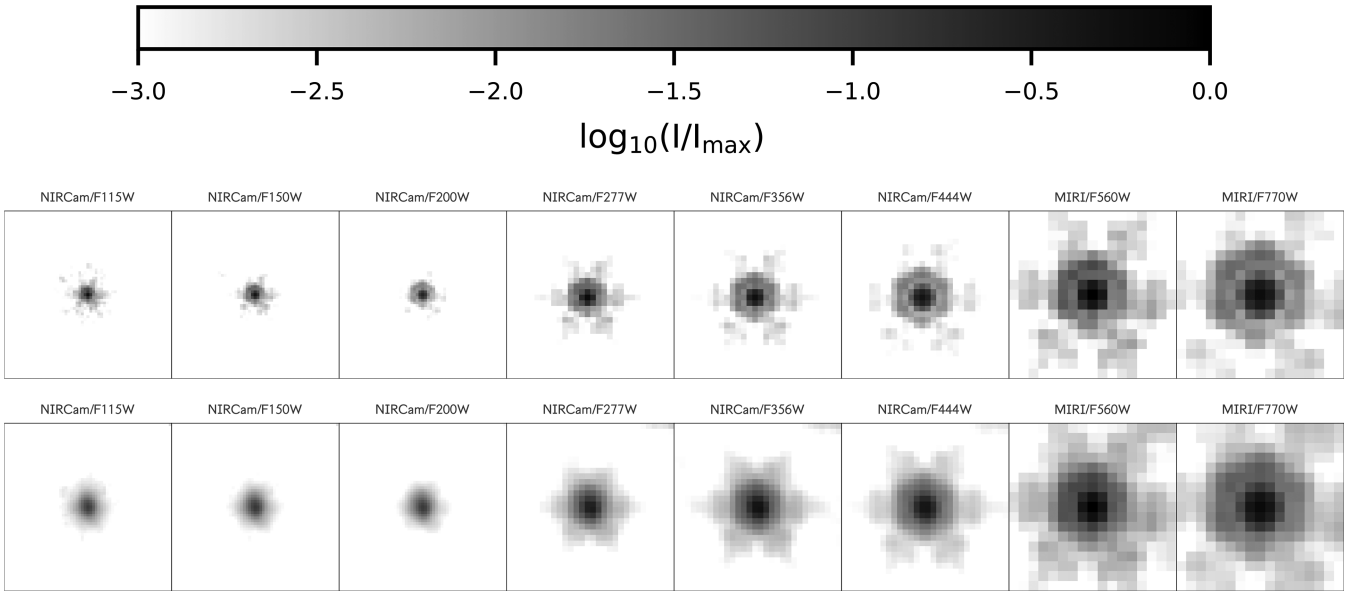

Figure 13. Intrinsic (no dust) mock *JWST* images. We show the host galaxy of the brightest quasar, plotting the distribution of intrinsic luminosities of star particles in NIRCam's F115W, F150W, F200W, F277W, F356W, F444W filters and MIRI's F560W, F770W filters. The images show a region of size 10 kpc in physical units, sampled at the *JWST* resolution and include the effects of the PSF. The top panel shows the images with the contribution from AGN luminosity included. The bottom-panel images do not have AGN. The intensity scale is logarithmic, varying from 0.1 per cent of the maximum intensity, $I_{\rm max}$, up to the maximum intensity, as indicated by the colour bar.

effective radius of $R_{\rm E} = 0.35$ kpc. This can be compared to the half-stellar mass radius, which is similar, 0.4 kpc. It is interesting that this host galaxy is among the most compact of all galaxies with stellar mass $\sim 10^{10}\,{\rm M}_{\odot}$ (see fig. 4 of Feng et al. 2015). We investigate the size distribution of galaxies and the relationship to their black holes in other work (Wilkins et al., in preparation).

Fig. 13 is similar to Fig. 12, but the band luminosities of the star particles are obtained from their intrinsic SEDs (i.e. without dust attenuation). As we have seen in the rest-frame UV images in Fig. 11, the intrinsic luminosity distribution of the galaxy is much more centrally concentrated. The dust attenuation towards the galaxy centre makes a large difference to the visual impression when comparing the bottom rows of Figs 13 and 12. The top rows including the AGN are barely affected on the other hand, showing again that point source subtraction will be important.

6.3 Composite image

In Fig. 14, we show a galaxy image where the star particles are colour coded by their respective luminosities in the *K* band, *V* band, and far-ultraviolet (FUV) band to form a red giant branch (RGB) composite image. The pixelization reflects the pixel resolution of 0.02 arcsec, but the image does not include PSF effects. The AGN is not included. The image is fairly featureless, with small colour gradients. We expect the host galaxy of the brightest quasar, J1342+0928, in B18 to have such an aspect when observed by *JWST*.

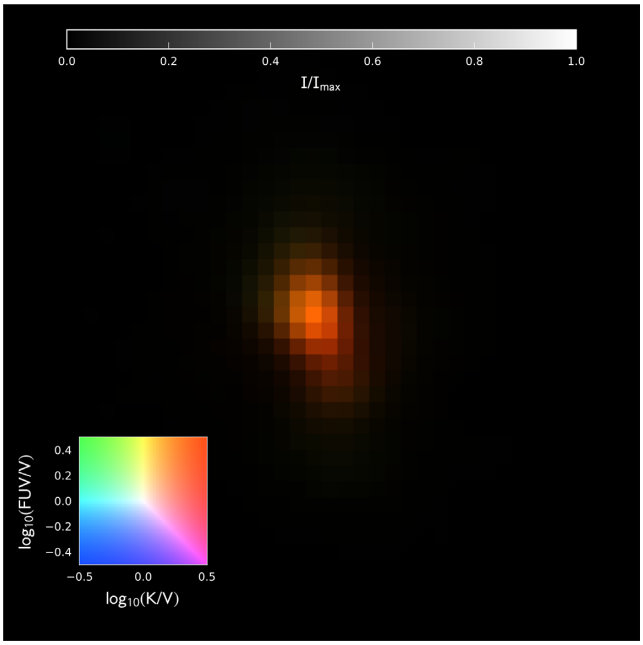

Figure 14. RGB image of the host galaxy of the brightest quasar in BT-II. We use the luminosities in the *K* band, *V* band, and FUV band to form the composite image. The full width of the plot is 4 kpc in physical units (corresponding to an angular size of 0.8 arcsec). Each pixel is 0.1 kpc in size. The inset shows the two-dimensional colour space for different values of FUV/*V* and *K*/*V*, where it is assumed that the brightest band is at the maximum intensity. The corresponding intensity scale when all the pixels have a flat spectrum (FUV = *V* = *K*) is also shown in the figure.

7 CONCLUSIONS

In this paper, we studied the properties of the host galaxy of the most luminous quasar in the BlueTides-II (BT-II) simulation at redshift $z \sim 7.5$. The first quasar observed at these redshifts was reported by B18. This quasar, J1342+0928, has a luminosity of $4 \times 10^{13}\,{\rm L}_{\odot}$ and black hole mass of $8 \times 10^{8}\,{\rm M}_{\odot}$. The volume and resolution of the

BT-II simulation makes it possible to study the properties of rare objects in the early Universe comparable to the B18 quasar. The brightest quasar in the simulation has a luminosity of $\sim 1.2 \times 10^{13}\,L_{\odot}$ and a black hole mass of $6.4 \times 10^{8}\,M_{\odot}$ at $z = 7.6$, which are comparable to those of the observed quasar, J1342+0928, in B18. However, the host galaxy properties of the observed quasar are not completely known, except for some constraints reported by Venemans et al. (2017) on the host dynamical mass ($<1.5 \times 10^{11}\,M_{\odot}$), star formation rate (85–545 $M_{\odot}\,yr^{-1}$), and dust mass ($\sim 10^{8}\,M_{\odot}$) using observations from IRAM/NOEMA and JVLA. *JWST* will make observational measurements of high-redshift galaxies including the J1342+0928 quasar of B18 in rest-frame optical/NIR wavelengths. Here, in addition to reporting the properties of the host galaxy of the brightest quasar in BT-II, we also make predictions for the properties of high-redshift galaxies based on their AGN luminosity. Further, we compare the spectral energy distributions of the galaxy with that of the underlying quasar and show mock images of the galaxy in *JWST* NIRCam and MIRI filters.

The most luminous quasar in BT-II is hosted by a galaxy of stellar mass $4 \times 10^{10}\,M_{\odot}$ and halo mass $1.2 \times 10^{12}\,M_{\odot}$. The SFR of the galaxy is $\sim 83\,M_{\odot}\,yr^{-1}$ at $z = 7.6$, with the SFR increasing by up to a factor of 2 as we move back to redshift $z = 8$. The host galaxy is one of the more massive galaxies at this redshift. However, this galaxy is not the most massive or luminous galaxy in BT-II. There are about 10 more galaxies in BT-II that are more massive than the host of the brightest quasar. From the UV magnitudes of the galaxies in the simulation, we find that the host galaxy is fainter by about 3 mag when compared to the brightest galaxies in BT-II. By comparing the mean metallicities of the galaxies and their AGN luminosity, we find that the host galaxy of the brightest quasar is among the galaxies with the highest metal content. Comparing our results with those of Venemans et al. (2017), we find that the predictions for stellar mass, SFR, and metal-enriched galaxy are consistent with the observational constraints. We also find that the galaxy is elliptical with a D/T ratio of 0.2 and is centred in a region with a low tidal field consistent with the findings in Di Matteo et al. (2017) for galaxies hosting the most massive black holes.

We computed the spectral energy distribution of the quasar and the host galaxy from the simulation data, to compare the relative monochromatic luminosities of the quasar and its host galaxy. Comparing the galaxy's dust-attenuated spectrum with its intrinsic spectrum, we find that the effect of dust decreases the luminosity by a factor of ∼5–10. The AGN is brighter than the dust-attenuated galaxy spectrum at all wavelengths and by a factor of 20–50 times in mid- and near-IR *JWST* bands.

Finally, we presented mock images of the host galaxy in *JWST* bands by taking into account the filter-dependent PSF effects and the pixelization corresponding to each *JWST* filter. The BT-II simulation has a resolution of ∼0.05 arcsec at $z = 7.6$, while *JWST* has an angular resolution of ∼0.1 arcsec. Given that the simulation resolution is well matched to that of *JWST*, BT-II is ideal to make predictions for the visual appearance of the host galaxy. We also looked at images showing the stellar distribution around the quasar, covering a region of size $4\,h^{-1}$ Mpc corresponding to *JWST*'s field of view, as well as studying the stellar distribution in the host galaxy without including PSF effects.

The prediction from BlueTides is that there are likely to be some companion galaxies in the *JWST* FOV around J1342+0928. In the particular example from the simulation that we have studied, there were two that were above the magnitude limit for reasonable *JWST* observations. As can be seen from Fig. 3, any that are seen are unlikely to host a bright AGN, and so there may an opportunity for galaxy imaging without the difficulties of point source subtraction. Turning to the host of the brightest BT-II quasar itself, by looking at the stellar images without PSF effects, we observe that the galaxy emission is visible up to ∼8 kpc from the quasar. The galaxy effective radius is however much less than this, $r_E = 0.35$ kpc. The galaxy surface brightness is fairly featureless with an ellipsoidal shape, consistent with the low kinematically measured D/T ratio. Point source subtraction of the AGN from the host galaxy images of the B18 quasar in *JWST* bands should be possible but will be challenging. This is because the AGN outshines the host galaxy by so much and because we expect the host galaxy to be extremely compact, even though it is as massive as the Milky Way. Follow-up *HST* observations of $z > 6$ quasars have been elusive at revealing the underlying UV stellar light of their host galaxies (e.g. Decarli et al. 2012; Mechtley et al. 2012). *JWST*'s exquisite sensitivity, resolution, and wide wavelength coverage will be essential (and hopefully sufficient) to constrain the stellar mass of these tiny host galaxies.

ACKNOWLEDGEMENTS

We acknowledge funding from NSFACI-1614853, NSF AST-1517593, NSF AST-1616168, NASA ATP NNX17AK56G, and NASA ATP 17-0123 and the BlueWaters PAID program. The BLUETIDES simulation was run on the BlueWaters facility at the National Center for Supercomputing Applications.

REFERENCES

Bañados E. et al., 2018, Nature, 553, 473 (B18)
Bertin E., Arnouts S., 1996, A&AS, 117, 393
Davis M., Efstathiou G., Frenk C. S., White S. D. M., 1985, ApJ, 292, 371
Decarli R. et al., 2012, ApJ, 756, 150
DeGraf C., Di Matteo T., Khandai N., Croft R., Lopez J., Springel V., 2012, MNRAS, 424, 1892
Di Matteo T., Springel V., Hernquist L., 2005, Nature, 433, 604
Di Matteo T., Khandai N., DeGraf C., Feng Y., Croft R. A. C., Lopez J., Springel V., 2012, ApJ, 745, L29
Di Matteo T., Croft R. A. C., Feng Y., Waters D., Wilkins S., 2017, MNRAS, 467, 4243
Eldridge J. J., Stanway E. R., Xiao L., McClelland L. A. S., Taylor G., Ng M., Greis S. M. L., Bray J. C., 2017, PASA, 34, e058
Fan X. et al., 2006, AJ, 132, 117
Feng Y., Di Matteo T., Croft R., Tenneti A., Bird S., Battaglia N., Wilkins S., 2015, ApJ, 808, L17
Feng Y., Di-Matteo T., Croft R. A., Bird S., Battaglia N., Wilkins S., 2016, MNRAS, 455, 2778
Ferland G. J. et al., 2013, RMxAA, 49, 137
Gardner J. P. et al., 2006, Space Sci. Rev., 123, 485
Governato F., Willman B., Mayer L., Brooks A., Stinson G., Valenzuela O., Wadsley J., Quinn T., 2007, MNRAS, 374, 1479
Hinshaw G. et al., 2013, ApJS, 208, 19
Hopkins P. F., 2013, MNRAS, 428, 2840
Jiang L. et al., 2009, AJ, 138, 305
Kalirai J., 2018, Contemp. Phys., 59, 251
Katz N., Quinn T., Bertschinger E., Gelb J. M., 1994, MNRAS, 270, L71
Katz N., Weinberg D. H., Hernquist L., 1996, ApJS, 105, 19
Khandai N., Feng Y., DeGraf C., Di Matteo T., Croft R. A. C., 2012, MNRAS, 423, 2397
Krumholz M. R., Gnedin N. Y., 2011, ApJ, 729, 36
Maiolino R. et al., 2005, A&A, 440, L51
Mechtley M. et al., 2012, ApJ, 756, L38
Mortlock D. J. et al., 2011, Nature, 474, 616
Ni Y., Di-Matteo T., Feng Y., Croft R. A., Tenneti A., 2018, MNRAS, 481, 4877

Okamoto T., Frenk C. S., Jenkins A., Theuns T., 2010, MNRAS, 406, 208
Perrin M. D., Long J., Sivaramakrishnan A., Lajoie C.-P., Elliot E., Pueyo L., Albert L., 2015, Astrophysics Source Code Library, record ASCL: 1504.007
Read J. I., Hayfield T., Agertz O., 2010, MNRAS, 405, 1513
Springel V., Hernquist L., 2003, MNRAS, 339, 289
Venemans B. P. et al., 2017, ApJ, 851, L8
Venemans B. P., Walter F., Zschaechner L., Decarli R., De Rosa G., Findlay J. R., McMahon R. G., Sutherland W. J., 2016, ApJ, 816, 37
Vogelsberger M. et al., 2014, MNRAS, 444, 1518
Vogelsberger M., Genel S., Sijacki D., Torrey P., Springel V., Hernquist L., 2013, MNRAS, 436, 3031
Volonteri M., Reines A. E., Atek H., Stark D. P., Trebitsch M., 2017, ApJ, 849, 155
Walter F. et al., 2003, Nature, 424, 406
Wang R. et al., 2011, AJ, 142, 101
Wang R. et al., 2013, ApJ, 773, 44
Waters D., Di Matteo T., Feng Y., Wilkins S. M., Croft R. A. C., 2016, MNRAS, 463, 3520
Wilkins S. M., Feng Y., Di-Matteo T., Croft R., Stanway E. R., Bunker A., Waters D., Lovell C., 2016, MNRAS, 460, 3170
Wilkins S. M., Feng Y., Di Matteo T., Croft R., Lovell C. C., Waters D., 2017, MNRAS, 469, 2517
Wu X.-B. et al., 2015, Nature, 518, 512

This paper has been typeset from a TEX/LATEX file prepared by the author.